ACS APPLIED MATERIALS & INTERFACES

Research Article

www.acsami.org

Directed Assembly of One- and Two-Dimensional Nanoparticle Arrays from Pulsed Laser Induced Dewetting of Square Waveforms

Nicholas A. Roberts,[†] Jason D. Fowlkes,[‡] Kyle Mahady,[§] Shahriar Afkhami,[§] Lou Kondic,[§] and Philip D. Rack*,[†,‡]

[†]Department of Materials Science and Engineering, University of Tennessee, Knoxville, Tennessee 37996, United States

[‡]Center for Nanophase Materials Sciences, Oak Ridge National Laboratory, Oak Ridge, Tennessee 37831, United States

[§]Department of Mathematical Sciences, New Jersey Institute of Technology, Newark, New Jersey 07102, United States

ABSTRACT: The directed assembly of arrayed nanoparticles is demonstrated by dictating the flow of a liquid phase filament on the nanosecond time scale. Results for the assembly of Ni nanoparticles on SiO_2 are presented. Previously, we have implemented a sinusoidal perturbation on the edge of a solid phase Ni, thin film strip to tailor nanoparticle assembly. Here, a nonlinear square waveform is explored. This waveform made it possible to expand the range of nanoparticle spacing−radius combinations attainable, which is otherwise limited by the underlying Rayleigh−Plateau type of instability. Simulations of full Navier−Stokes equations based on volume of fluid method were implemented to gain further insight regarding the nature of instability mechanism leading to particle formation in experiments.

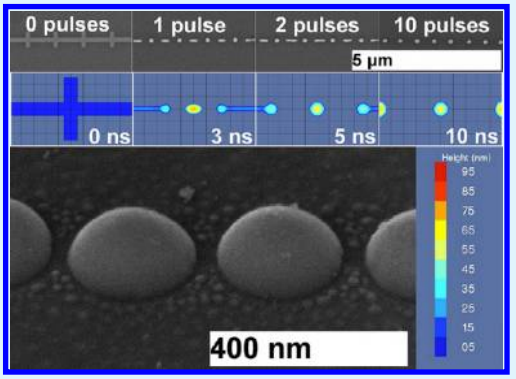

KEYWORDS: *pulsed laser induced dewetting, directed assembly*

INTRODUCTION

Self-assembly provides a pathway to extend the applicability of conventional lithography methods, such as photolithography and electron beam lithography (EBL) beyond current limitations. Further reductions in nanostructure spacing and the assembly of three-dimensional architectures may be possible with such methods. Regarding applications, well-ordered and controlled arrays of nanoparticles in one- and two-dimensions are becoming increasingly important for plasmonic applications where optoelectronic device sizes could be reduced or for use in creating plasmonic waveguides, lenses, light generators, and switches.[1] Applications also include magnetic data storage with arrays of magnetic nanoparticles, where a need to increase densities is apparent.[1] Criteria for these applications typically require very small and closely spaced nanoparticles. Additionally, the ability to control the location and size of spherical nanoparticles is of particular interest in the catalyst community for fuel cell development.[2] Catalytically induced nanowire and nanotube growth from metallic catalyst with controllable orientation and geometry has also been demonstrated.[3−5] Current top-down nanofabrication techniques are prone to proximity limitations, and thus new methods are being explored, including work in the self- and directed-assembly of arrays of particles. In addition to the requirement of small and closely spaced particles, there is a focus on creating rounded particles, which cannot be done with current top-down or line-of-sight deposition techniques without additional processing.

Pulsed laser induced dewetting (PLiD) in the liquid-phase,[6−18] as well as solid-phase dewetting,[19−26] of continuous and patterned thin metallic films is one area that is actively being explored and that holds promise for creating well order and controlled arrays of metallic particles. Giermann and Thompson also demonstrated ordered two-dimensional arrays of Au particles by templating the substrate to form vias as pockets for the diffusing metal to collect.[17,22] Similarly, Sundar et al.[23] and Farzinpur et al.[28] have also demonstrated the ability to control two-dimensional particle spacings using templated solid-phase dewetting methods. Brasjen et al. has also demonstrated a templating method via chemically modifying the substrate instead of a physical templating to direct the dewetting process.[25] Additionally, Fowlkes et al.,[11] Wu et al.,[12,14] and Ye and Thompson[20] have created interesting nanoparticle structures and compositions with different lithographically patterned geometries. Krishna et al. and Sachan et al. recently demonstrated a self-organization of bilayer metallic films resulting in controllable pattern characteristics.[26,27] Recent work by Cho et al. has also demonstrated the ability to fold two-dimensionally patterned features into three-dimensional shapes in a process similar to dewetting.[28]

Fowlkes et al. recently demonstrated high fidelity Ni particles derived from thin film strips with imposed, nanoscale sinusoidal perturbations to drive the formation of linear particle arrays by

Received: March 13, 2013
Accepted: April 22, 2013
Published: April 22, 2013

engaging a process similar to the Rayleigh–Plateau fluid instability (referred to as RP instability in what follows for simplicity).[13] A central feature of the self-assembly approach is the development of the RP fluid instability of a liquid filament (also referred to as a rivulet) which leads to transition between the initial solid strip and final particle ensemble.[10]

In this work we demonstrate directed-assembly using a nonlinear, square waveform to yield a more diverse range of metallic nanoparticles arrays on substrates with well-controlled particle sizes and particle-to-particle spacing. Specifically, we introduce the use of variable square wave synthetic perturbations to develop highly ordered and uniform particles in one- and two-dimensions via pulsed laser induced dewetting; we thus use a confluence of top-down electron beam lithographically patterned structures and the subsequent bottom-up directed-assembly to realize geometries at or below the resolution of the stand alone lithography pattern. In addition, we carry out full Navier–Stokes simulations, which provide additional insight regarding the details of the directed-assembly observed in experiments.

NANOSTRUCTURE SYNTHESIS

PMMA 495 A4 was spin-coated onto a 100 nm SiO_x/Si wafer at 4000 rpm for 45 s followed by a softbake at 180 °C for 2 min. The exposure was performed using a JEOL 9300 electron beam lithography system with a 100 kV acceleration voltage and 2 nA beam current. The exposure dose for the patterns was 1000 $\mu C/cm^2$. The exposed patterns were developed for 100 s in MIBK/IPA at a 1:3 ratio mixture, rinsed with IPA, and dried with N_2 gas. Microwave plasma "descum" was performed to remove any residual organics in the patterned areas. 7 ± 1 nm to 11 ± 1 nm of Ni was DC Magnetron sputtered at a rate of 3.97 nm/min. Ni is used here to demonstrate the technique, but there are many metal/substrate combinations that are compatible for this process. The unexposed resist was then lifted off in an acetone bath via ultrasonication. The resulting patterns were then exposed to a 248 nm KrF laser with an 18 ns full-width-at-half-maximum pulse widths at a fluence of 210 ± 10 mJ/cm^2 for a total of 10 noninteracting pulses at a frequency of 5 Hz. The laser fluence is sufficient enough to melt the nickel film for an estimated 22 ns liquid lifetime per pulse. The pulsed laser results in rapid melting and resolidification of the patterned Ni films and has been previously shown,[10,13] the transport in the liquid phase dominates and therefore liquid phase assembly is attributed to the nanoparticle array formation.[10]

Pulsed laser induced dewetting of patterned lines with square wave perturbations is investigated by varying the perturbation wavelength, amplitude, and width. We also investigate the transition from one-dimensional linear arrays to producing two-dimensional ordered arrays of nanoparticles. Figure 1 illustrates the parameters and nomenclature investigated for the one-dimensional square wave perturbation and subsequent nanoparticle arrays.

RESULTS

Thin film strip (Figure 1, blue) melting results in the formation of a substrate supported liquid jet, or filament (Figure 1, green), which wets the underlying substrate. The liquid geometry that results is of a semicylindrical cross-section characterized by its mean radius R_o, owing to capillary forces. The cylinder is truncated by the underlying substrate yielding a characteristic wetting angle Θ due to interaction forces between the liquid metal and the supporting, SiO_2 film. The filament is prone to break up (fragment) into droplets (Figure 1, red), by RP instability mechanism, once this geometry has formed.

Filament fragmentation proceeds by the process of growth of varicose waves that spontaneously form and grow in amplitude in the normal direction (perpendicular to the long axis of the

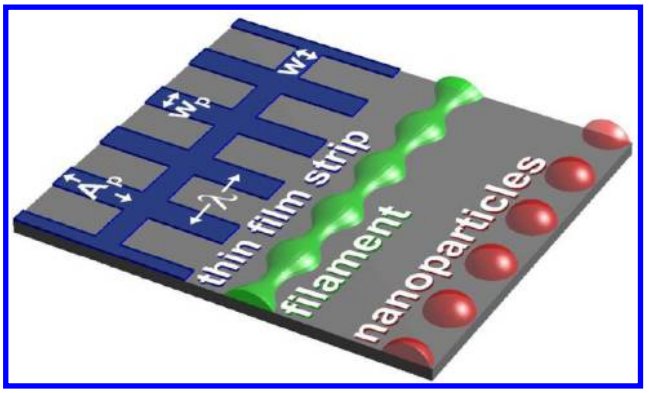

Figure 1. Schematic of the as-deposited patterned metal thin film strip with edge-defined square wave perturbations (blue), the liquid filament (green) formed after nanosecond pulsed laser induced melting and the resulting, resolidified spherical nanoparticles formed after irradiation (red). The underlying, solid substrate is shown in greyscale.

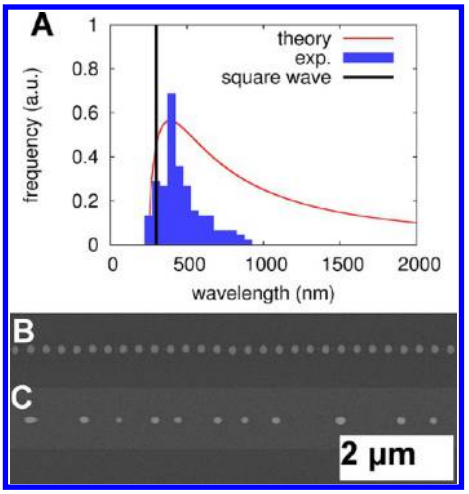

Figure 2. (a) The dispersion curve obtained based on the RP instability mechanism ((red) solid curve), along with the distribution of particle spacing obtained using line with a square wave perturbation of A_p = 295.8 ± 5 nm, w_p = 112 ± 5 nm, w = 112 ± 5 nm, λ = 300 nm, and a thickness of 7 ± 1 nm. (b-c) SEM images of the resulting particles from the square wave perturbed line and the unperturbed line of equivalent volume.

filament). Such a varicose mode is shown schematically in Figure 1 (green) superimposed on the filament itself. The growth rate of such a varicose wave strongly depends on its wavelength. Figure 2a shows the dispersion curve,[13] capturing this relationship, where the growth rate of a given wave is plotted versus its wavelength. Positive values of the growth rate correspond to unstable RP modes, while negative values (not shown on this plot) represent stable RP modes. The wavelength at a zero growth rate is known as the critical wavelength for the system. For the purpose of comparison discussed later in the paper, the growth rate units have been omitted from the vertical axis in favor of normalizing the dispersion curve with respect to the final spacing (blue) histogram of the nanoparticles, showing the distribution of first nearest neighbor spacing resulting from the melting of a *straight-edged*, thin film strip. This form of overlay reveals the close relationship between the fastest growing perturbations (modes) (large, positive values of the dispersion curve) and the

dx.doi.org/10.1021/am400925h | ACS Appl. Mater. Interfaces 2013, 5, 4450–4456

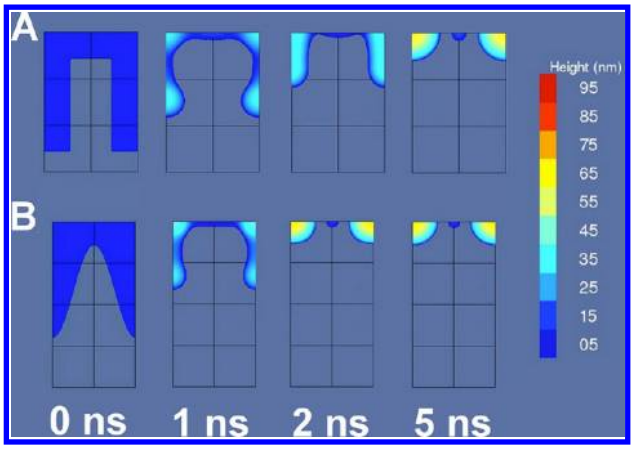

Figure 3. Comparison of simulations of dewetting evolution for 200 nm wavelength (a) square wave and (b) sinusoidal perturbations (A_p = 200 nm, w_p = 112 nm, w = 112 nm, λ = 200 nm, and a thickness of 7 nm). A single perturbation period is simulated; the domain boundaries also serve as lines of symmetry. Each box corresponds to 100 nm.

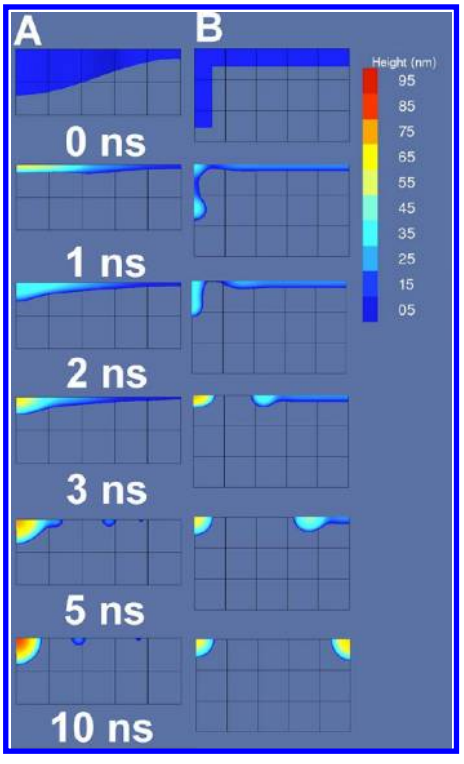

Figure 4. Comparison of simulations of dewetting evolution for 1000 nm wavelength (a) sinusoidal and (b) square wave perturbations (A_p = 200 nm, w_p = 112 nm, w = 112 nm, λ = 1000 nm, and a thickness of 7 nm). One half of a perturbation period is simulated for efficiency; the domain boundaries also serve as lines of symmetry. Each box corresponds to 100 nm.

final nanoparticle spacing. We note that a liquid filament is prone to breakup by a *host* of competing varicose waves as evidenced both by the breadth of the dispersion curve around the maximum value and the corresponding breadth of the final pitch histogram. Peak alignment between the histogram maximum and dispersion curve further supports the relationship between final particle spacing and the perturbation growth rate. The wavelength for which the growth rate is maximized is

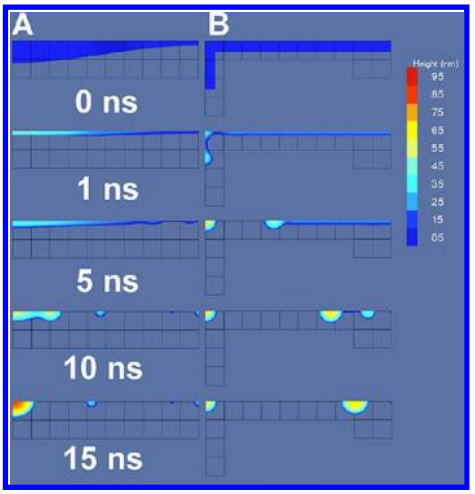

Figure 5. Comparison of simulations of dewetting evolution for 2000 nm wavelength (a) sinusoidal and (b) square wave perturbations (A_p = 200 nm, w_p = 112 nm, w = 112 nm, λ = 2000 nm, and a thickness of 7 nm). A single perturbation period is simulated; the domain boundaries also serve as lines of symmetry. Each box corresponds to 100 nm.

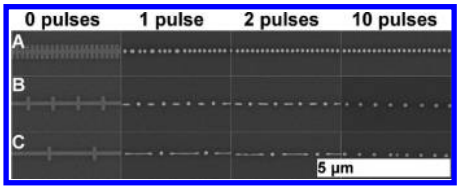

Figure 6. SEM images of the experimental evolution of the pinch-off and final particle distribution of the square wave perturbations as a function of the number of pulses at 160 mJ/cm^2 (A_p = 200 nm, w_p = 112 nm, w = 112 nm, and a thickness of 7 nm) for (a) λ = 200 nm, (b) λ = 1000 nm, and (c) λ = 2000 nm.

a characteristic feature of the nanoparticle formation process and is often referred to as the wavelength of maximum growth.

In the previous work, we have demonstrated the ability to tailor the final nanoparticle spacing by imposing a specific waveform on the liquid filament.[13] This predefined waveform is patterned onto the edge of the original thin film strip during the EBL exposure pattern step. Remarkably, this imposed waveform evolves to axial modulations of the liquid filament after the solid-to-liquid phase transformation. We have shown that such a mode completely dictates filament fragmentation, even if it has a relatively small growth rate relative to the maximum growth rate predicted by the dispersion curve. Exponential growth rates favor the evolution of any unstable mode provided a nonvanishing amplitude is imposed. For example, the vertical, black line indicates that the particle spacing for a square wave strip (the perturbation amplitude (A_p) 295 nm, the perturbation width (w_p) 112 nm, the line width (w) 112 nm, and the wavelength (λ) 300 nm) corresponds exactly to the imposed wavelength. Figure 2b shows an SEM image of the discrete nature of the final nanoparticle spacing derived from the square wave, relative to a strip of the same volume patterned without a perturbation (Figure 2c).

Square Wave Perturbations Are Explored in This Work with the Goal of Expanding the Nanoparticle Spacing–Volume Space Attainable by Directed Assembly but Which Is Constrained by the Nature of Rayleigh–Plateau Instability. While we previously demonstrated that small amplitude, sinusoidal perturbations lead to

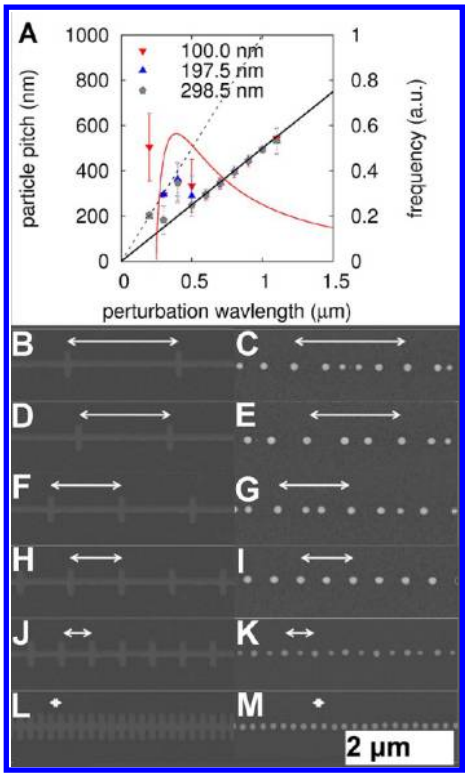

Figure 7. (a) Distance between nanoparticles (center-to-center) as a function of the perturbation wavelength for different perturbation amplitudes for initial strip of a thickness of 7 ± 1 nm. The dashed black line corresponds to the spacing of particles at the node locations only. The solid black line corresponds to the spacing for particles at the node locations and at the midpoint between the perturbations. The solid red line corresponds to the RP distribution on the right axis. (b-m) SEM images of initial and final configurations. (b-c) λ = 2 μm. (d-e) λ = 1.5 μm. (f-g) λ = 1.2 μm. (h-i) λ = 800 nm. (j-k) λ = 500 nm. (l-m) λ = 200 nm.

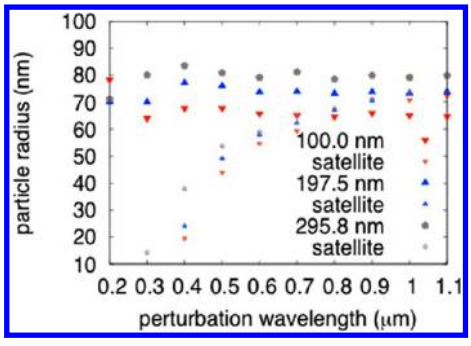

Figure 8. Node and satellite particle radii as a function of the perturbation wavelength for different perturbation amplitudes (A_p = 100 nm, 197.5 nm, and 295.8 nm) for a film thickness of 7 ± 1 nm.

directed-assembly, nanoparticle spacings below the critical wavelength of the dispersion curve are forbidden because modes in this wavelength range are stable, e.g., ~<250 nm in Figure 2a (where the red dispersion curve intersects the *x*-axis). Stable modes essentially disappear with time. Here, we attempt to avoid this limitation and produce nanoparticles within the 'forbidden' range set by the RP model, by imposing larger, nonlinear waveforms on the initial strip edge. It should be noted, however, that the waveform itself contributes significantly to the total filament volume. Thus, it is not obvious how to define a "filament" radius and hence estimate the dispersion

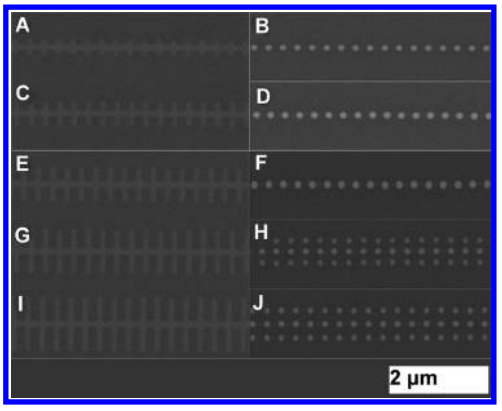

Figure 9. SEM images of the amplitude of the perturbation and the resulting nanoparticle array for a film thickness of 7 ± 1 nm and λ = 300 nm. (a-b) A_p = 100.0 nm. (c-d) A_p = 197.5 nm. (e-f) A_p = 295.8 nm. (g-h) A_p = 393.2 nm. (i-j) A_p = 490.0 nm.

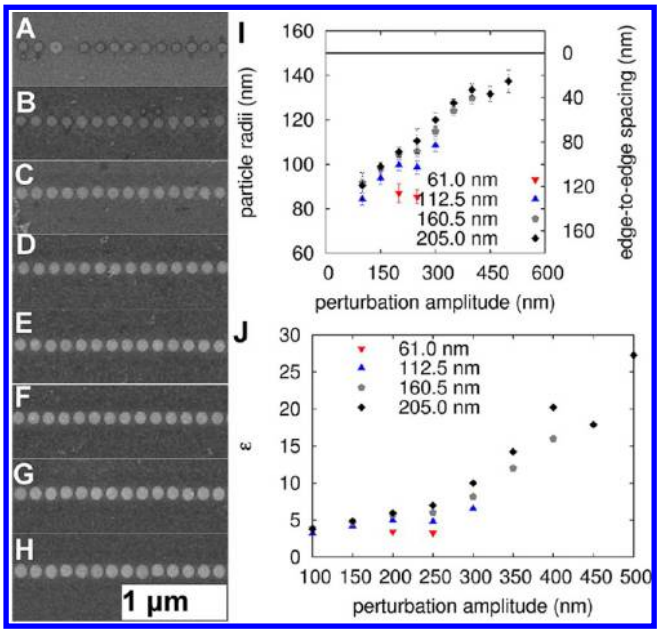

Figure 10. SEM images of pulsed laser induced particle arrays from square wave perturbations (λ = 300 ± 5 nm, A_p = 295.8 ± 5 nm, and a 11 ± 1 nm thickness) with a variable perturbation width. (a) w_p = 27 ± 5 nm, (b) w_p = 61 ± 5 nm, (c) w_p = 81 ± 5 nm, (d) w_p = 112 ± 5 nm, (e) w_p = 132 ± 5 nm, (f) w_p = 160.5 ± 5 nm, (g) w_p = 181 ± 5 nm, and (h) w_p = 205 ± 5 nm. (i) Particle radii and edge-to-edge particle spacing as a function of perturbation amplitude for different perturbation widths. (j) Dimensionless plasmonic coupling parameter as a function of the perturbation amplitude for different perturbation widths.

curve. As a baseline for comparison with the RP predictions, we have chosen to define an "effective filament radius", R_{eff}, which assumes that the volume of metal (V) contained within one strip λ is converted into a filament. The effective filament radius is related to the wetting angle of the filament, the wavelength of the strip perturbation, and the volume:

$$R_{eff} = \sqrt{\frac{V}{\lambda(\theta - \sin\theta\cos\theta)}} \quad (1)$$

Subsequently, the RP dispersion curve is calculated based on R_{eff}. It should be understood that assertions made regarding the stability of the effective filament are made within the context of

dx.doi.org/10.1021/am400925h | ACS Appl. Mater. Interfaces 2013, 5, 4450−4456

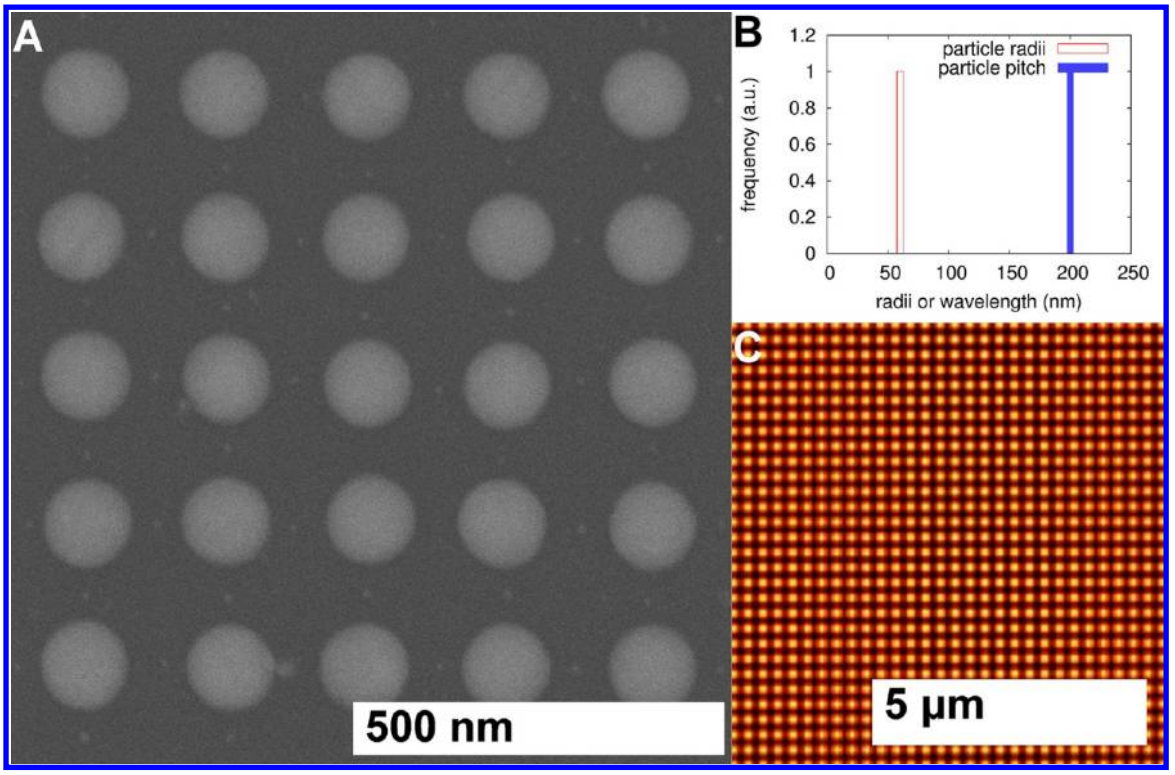

Figure 11. (a) SEM image of the resulting nanoparticle array from a two-dimensional mesh structure with a line width of $w = 129 \pm 5$ nm, a pitch of $\lambda = 200 \pm 5$ nm in both dimensions, and a 7 ± 1 nm thickness. (b) Particle radii and particle pitch histograms from a 10 μm × 10 μm area of the array shown in (a). (c) Spatial Correlation Function results of the array shown in (a).

the RP theory while mindful that the underlying physics may deviate owing to the nonlinear waveform imposed. Thus, the RP mechanism is used only as a reference frame through which results may be interpreted.

Further insight regarding evolution of dewetting can be obtained by simulations. For this purpose, we have used a volume-of-fluid (VoF) based flow solver, implemented in an open source package.[29,30] VoF solvers have been used previously to successfully predict the breakup of thin films into arrays of axisymmetric particles.[31] Briefly, we numerically solve the incompressible, Newtonian, two-phase Navier−Stokes equations with surface tension in three dimensions using the material parameters corresponding to the experimental ones. A Navier slip boundary condition (with slip length of 60 nm) has been used at the metal/solid interface. More details about implementation of VoF in the context of liquid metals can be found in Afkhami and Kondic.[32] In the present work, we use the simulations in particular to analyze in more detail the differences between sinusoidal and square-wave perturbations. The comparison is carried out by considering a constant film thickness of 7 nm for perturbation wavelengths of 200 nm, 1000 nm, and 2000 nm. The simulations with either sinusoidal or square wave perturbations assume the same (constant) fluid volume, and therefore different amplitudes and central strip widths are necessary for geometrical reasons. Figures 3, 4, and 5 show the results of simulations. For the short wavelength (Figure 3), no discernible difference is observed, but for longer wavelengths (Figures 4 and 5) a distinct difference in the evolution is found. For the sinusoidal perturbations, retraction of the peak is observed, and the time scale for the initial filament pinch-off is much slower. Interestingly, the pinch-off occurs at the sinusoid trough and axial retraction and secondary particles form depending on the wavelength. For the square wave, the pinch-off occurs at the node (near the perturbation itself), and then the remaining fluid flows away from the node particle. We note that the secondary particle distribution differs for the sinusoidal perturbation versus the equal-volume square wave. Figure 4 shows that the square wave perturbation maintains a periodic array in the 1000 nm wavelength case, while the sinusoidal perturbation results in a single particle at the peak and multiple small particles in between. For the 2000 nm wavelength (Figure 5) again the initial pinch-off occurs in the peak region for the square wave and the trough for the sinusoidal perturbation and the number and size of the secondary particles are different. For comparison, Figure 6 shows SEM images of the evolution of the square wave perturbations with wavelengths of 200 nm, 1000 nm, and 2000 nm. Excellent agreement is observed between simulations and experiments with both the time and location of the initial filament pinch-off as well as the final particle distribution. Additionally, the simulations of the sinusoidal perturbations shown in Figures 3, 4, and 5 agree well with experimental observations of the breakup from ref 33, with albeit slightly different geometries.

Subsequent to the time-dependent study, we investigate in more detail the resultant nanoparticle assembly as a function of various square wave parameters. Figure 7b-m shows SEM images of nanoparticle arrays obtained by imposing different square wave perturbation wavelengths. At short wavelengths, the nanoparticle arrays consist of a single particle correlated to the square wave perturbation location (node), while at longer wavelengths secondary particles of variable size begin forming between the nodes, thus enabling the ability to define nanoparticles below the resolution limits of EBL. The size of these satellite particles grows with increasing perturbation wavelength. We note that the RP instability has been known to

yield satellite droplets in the case of a fluid jet suspended in vapor,[34] or for millimeter sized glycerin filaments,[35] consistent with our observations. The transition to more than one particle per perturbation wavelength is observed as the wavelength approaches two times that of the mode of maximum growth (λ_m) from the RP instability. The initial stages of this process are observed as small satellite particles that form between the node particles even at short wavelengths. As the perturbation wavelength increases even further, dispersion in the internodal particles increases as the natural RP instability is observed. Figure 7a shows the average particle spacing or pitch of 90 μm long strips as a function of the perturbation wavelength for different perturbation amplitudes. The dashed and solid lines in Figure 7a illustrate one and two particles per perturbation, respectively, as a function of the perturbation wavelength. Figure 7 also shows the RP dispersion curve (red curve corresponding to the right vertical axis) as a function of wavelength for an unperturbed line with equivalent volume for the 112 ± 5 nm wide and 296 ± 5 nm tall perturbations. The comparison demonstrates our ability to achieve particle spacing in the "stable" RP regime as well as control precisely the particle spacing even at wavelengths which are very close to the critical one (where stability according to RP mechanism changes from stable to unstable).

Figure 8 shows the average particle size as a function of the perturbation wavelength for various perturbation amplitudes. As discussed above, at short wavelengths no satellite particles are observed. As the perturbation wavelength is increased, satellite particles begin to form; at this point no change in the node particle size is observed. The constant size of the node particle is due to the instability of the square wave perturbation. Since the time scale is much faster for the synthetic instability, the node particles are formed first, and the size is dictated by the volume of the perturbation (amplitude in this case). At short wavelengths the node particle size varies to a certain degree because of the competition for material from adjacent nodes. When the nodes are sufficiently far apart to form a satellite particle, they saturate at a critical size. At longer wavelengths the satellite particles continue to grow until the distance between the nodes is large enough (λ > 1.2 μm) to form multiple particles, as expected based on RP instability mechanism. The process leading to formation of satellite droplets is clearly seen in the simulation results as well. In particular, the simulations confirm the difference in the time scales regarding formation of node particles versus slower process of satellite formation (see Figures 4 and 5).

In addition to controlling the particle spacing, the particle size is also of significant importance. For fixed center-to-center particle spacing the edge-to-edge spacing of the particles can be adjusted by changing the size of the resulting particles. The patterned square wave approach allows for particle size adjustments by modifying the baseline width, the film thickness, perturbation amplitude, or perturbation width, defined in Figure 1. In the present work, we will concentrate on changing the amplitude and width of the square wave to explore the limits of how large these quantities can be while still forming a one-dimensional array of particles. Based on RP instability mechanism, now applied to a perturbation itself, we expect that there are limits on the relative size of these quantities that still results in a single particle in the direction perpendicular to the strip itself ($A_p < \lambda_m$). Since λ_m is related to the line width and thickness for a line the same can be assumed for the perturbation since the geometry of the perturbation is similar to a line. Based on this assumption, the maximum perturbation amplitude can increase as the perturbation width increases (mitigating breakup along the direction perpendicular to the filament axis). Based on this qualitative argument, we demonstrate how the perturbation amplitude changes the resulting particle properties.

Figure 9 shows SEM images of particle arrays for fixed perturbation width of 112 ± 5 nm and wavelength of 300 ± 5 nm, while the perturbation amplitude is varied from 100 ± 5 nm to 512 ± 5 nm. The resulting particles maintain a fixed pitch, while the particle size varies due to the change of the perturbation volume. When the amplitude becomes too large (>300 nm), multiple particles form along the perturbation axis. Within the limit of available amplitudes we then investigate the role that the combined amplitude and perturbation width has on the particle sizes.

For the discussed applications of these one-dimensional arrays of particles, the goal is to create closely spaced particles. To explore how close we can obtain particles within an array we vary the perturbation width in addition to the perturbation amplitude, and in particular we introduce additional volume with the goal of creating larger particles at a fixed perturbation wavelength. In these experiments the film thickness is 11 ± 1 nm. This increased thickness also increases the volume and results in larger particles. Additionally, the increased thickness is expected to increase the critical wavelength, therefore limiting how short our perturbation wavelength can be. In this experiment we fix the perturbation wavelength at 300 nm and the perturbation amplitude at 300 nm and vary the perturbation width to explore how small we could tune the edge-to-edge particle distance. Figure 10a-h shows SEM images of particle arrays for fixed perturbation amplitude and wavelength with varying perturbation width. Similarly to the perturbation amplitude, with increasing perturbation width the particle pitch remains constant while the particle size increases, resulting in closer spaced particles. Figure 10i shows the average particle size and edge-to-edge spacing as a function of the perturbation amplitude for multiple perturbation widths.

For many applications both the particle size and spacing are of interest. Plasmonic coupling in particular has been shown to occur between two Au nanoparticles when the spacing is less than 2.5 times the diameter of the particle.[36] To determine the quality (combination of both size and spacing) we introduce the following parameter of merit

$$\varepsilon \equiv 2.5 \times d/g \qquad ([2])$$

where d is the particle diameter, and g is the length of the gap between particles (pitch minus diameter). Figure 10j shows ε as a function of amplitude for various perturbation widths. The increased perturbation amplitude and width result in increases in particle size and a minimum spacing on the order of 10 ± 4 nm. An ε of greater than 1 is expected to exhibit plasmonic coupling between two particles.

With understanding of the dewetting behavior of these one-dimensional patterns, the basic principles can be extended to a two-dimensional array of nanoparticles by intersecting the one-dimensional arrays. Figure 11 shows an SEM image of the two-dimensional array of nanoparticles along with a histogram of the particle size and spacing as well as the spatial correlation function of the image. The image of the spatial correlation function in Figure 11c demonstrates the symmetry and order of the 2-dimensional particle array shown in Figure 11a.

CONCLUSIONS

Square wave perturbations of varying width and amplitude are used to produce highly ordered one-dimensional arrays of nickel particles with excellent control over the particle size and pitch that is below the one obtained by traditional top-down methods. Both experiments and simulations of Navier–Stokes equations show that the mechanism leading to formation of the particle arrays is influenced strongly by the geometrical properties of the imposed perturbations. Translation to two-dimensional arrays is also demonstrated for a subset of the variables considered in the one-dimensional case.

AUTHOR INFORMATION

Corresponding Author

*E-mail: prack@utk.edu.

Author Contributions

The manuscript was written through contributions of all authors. All authors have given approval to the final version of the manuscript. N.A.R., J.D.F., and P.D.R contributed all experimental results, and K.M., S.A., and L.K contributed all simulation results.

Notes

The authors declare no competing financial interest.

ACKNOWLEDGMENTS

J. Fowlkes acknowledges support from the U.S. Department of Energy, Basic Energy Sciences, Materials Sciences and Engineering Division for sponsoring the aspects of this work related to understanding the fundamental mechanisms operative during liquid phase, thin film dewetting. P. Rack and L. Kondic acknowledge partial support by the U.S. Department of Energy, Basic Energy Sciences, Materials Sciences and Engineering Division NSF Grant No. CBET 1235710. A portion of this work was conducted at the Center for Nanophase Materials Sciences, which is sponsored at Oak Ridge National Laboratory by the Office of Basic Energy Sciences, U.S. Department of Energy. The authors acknowledge many useful and insightful discussions with Javier Diez and Alejandro Gonzalez of Universidad Nacional del Centro de la Provincia de Buenos Aries, Argentina.

ABBREVIATIONS

EBL = electron beam lithography
PLiD = pulsed laser induced dewetting
RP = Rayleigh–Plateau
SEM = scanning electron microscopy
VoF = volume of fluids

REFERENCES

(1) Nie, Z.; Petukhova, A.; Kumacheva, E. *Nat. Nanotechnol.* **2010**, *5*, 15–25.
(2) Kumar, A.; Ciucci, F.; Morozovska, A. N.; Kalinin, S. V.; Jesse, S. *Nat. Chem.* **2011**, *3*, 707.
(3) Guan, Y. F.; Pearce, R. C.; Melechko, A. V.; Hensley, D. K.; Simpson, M. L.; Rack, P. D. *Nanotechnology* **2008**, *19*, 235604.
(4) Melechko, A. V.; Klein, K. L.; Fowlkes, J. D.; Hensley, D. K.; Merkulov, I. A.; McKnight, T. E.; Rack, P. D.; Horton, J. A.; Simpson, M. L. *J. Appl. Phys.* **2007**, *102*, 074314.
(5) Fowlkes, J. D.; Melechko, A. V.; Klein, K. L.; Rack, P. D.; Smith, D. A.; Hensley, D. K.; Doktycz, M. J.; Simpson, M. L. *Carbon* **2006**, *44*, 1503.
(6) Bischof, J.; Scherer, D.; Herminghaus, S.; Leider, P. *Phys. Rev. Lett.* **1996**, *77*, 1536.
(7) Herminghaus, S.; Jacobs, K.; Mecke, K.; Bischof, J.; Fery, A.; Ibn-Elhaj, M.; Schlagowski, S. *Science* **1998**, *282*, 916.
(8) Favazza, C.; Trice, J.; Gangopadhyay, A. K.; Garcia, H.; Sureshkumar, R.; Kalyanaraman, R. *J. Electron. Mater.* **2006**, *35*, 1618.
(9) Trice, J.; Thomas, D.; Favazza, C.; Sureshkumar, R.; Kalyanaraman, R. *Phys. Rev. B* **2007**, *75*, 235439.
(10) Kondic, L.; Diez, J. A.; Rack, P. D.; Guan, Y.; Fowlkes, J. D. *Phys. Rev. E* **2009**, *79*, 026302.
(11) Fowlkes, J. D.; Wu, Y.; Rack, P. D. *ACS Appl. Mater. Interfaces* **2010**, *2*, 2153.
(12) Wu, Y.; Fowlkes, J. D.; Rack, P. D.; Diez, J. A.; Kondic, L. *Langmuir* **2010**, *26*, 11972.
(13) Fowlkes, J. D.; Kondic, L.; Diez, J.; Wu, Y.; Rack, P. D. *Nano Lett.* **2011**, *11*, 2478.
(14) Wu, Y.; Fowlkes, J. D.; Roberts, N. A.; Diez, J. A.; Kondic, L.; Gonzalez, A. G.; Rack, P. D. *Langmuir* **2011**, *27*, 13314.
(15) Ruffino, F.; Carria, E.; Kimiagar, S.; Crupi, I.; Simone, F.; Grimaldi, M. G. *Sci. Adv. Mat.* **2012**, *4*, 708.
(16) Ma, M.; He, Z.; Yang, J.; Chen, F.; Wang, K.; Zhang, Q.; Deng, H.; Fu, Q. *Langmuir* **2011**, *27*, 13072.
(17) Giermann, A. L.; Thompson, C. V. *Appl. Phys. Lett.* **2005**, *86*, 1903.
(18) Kim, D.; Giermann, A. L.; Thompson, C. V. *Appl. Phys. Lett.* **2009**, *95*, 1903.
(19) Oh, Y.-J.; Ross, C. A.; Jung, Y. S.; Wang, Y.; Thompson, C. V. *Small* **2009**, *5*, 860.
(20) Ye, J.; Thompson, C. V. *Phys. Rev. B* **2010**, *82*, 3408.
(21) Clearfield, R.; Railsback, J. G.; Pearce, R. C.; Hensley, D. K.; Fowlkes, J. D.; Fuentes-Cabrera, M.; Simpson, M. L.; Rack, P. D.; Melechko, A. V. *Appl. Phys. Lett.* **2010**, *97*, 3101.
(22) Giermann, A. L.; Thompson, C. V. *J. Appl. Phys.* **2011**, *109*, 3520.
(23) Sundar, A.; Decker, C.; Hughes, R. A.; Neretina, S. *Mater. Lett.* **2012**, *76*, 155.
(24) Farzinpour, P.; Sundar, A.; Gilroy, K. D.; Eskin, Z. E.; Hughes, R. A.; Neretina, S. *Nanoscale* **2013**, *5*, 1929.
(25) Brasjen, B. J.; Gu, H.; Darhuber, A. A. *Microfluid Nanofluid* **2013**, *14*, 669.
(26) Krishna, H.; Shirato, N.; Yadavali, S.; Sachan, R.; Strader, J.; Kalyanaraman, R. *ACS Nano* **2011**, *5*, 470.
(27) Sachan, R.; Yadavali, S.; Shirato, N.; Krishna, H.; Ramos, V.; Duscher, G.; Pennycook, S. J.; Gangopadhyay, A. K.; Garcia, H.; Kalyanaraman, R. *Nanotechnology* **2012**, *23*, 275604.
(28) Cho, J.-H.; Keung, M. D.; Verellen, N.; Lagae, L.; Moshchalkov, V. V.; Van Dorpe, P.; Gracias, D. H. *Small* **2011**, *7*, 1943.
(29) Popinet, S. *J. Comput. Phys.* **2009**, *228*, 5838.
(30) Popinet, S. 2012; *Version 1.3.2*. http://gfs.sourceforge.net (accessed May 1, 2013).
(31) Mead-Hunter, R.; King, A. J. C.; Mullins, B. J. *Langmuir* **2012**, *28*, 6731.
(32) Afkhami, S.; Kondic, L. *arXiv:1303.1562* 2013.
(33) Fowlkes, J. D.; Kondic, L.; Diez, J. A.; Gonzalez, A. G.; Wu, Y.; Roberts, N. A.; McCold, C. E.; Rack, P. D. *Nanoscale* **2012**, *4*, 7376.
(34) Eggers, J.; Villermaux, E. *Rep. Prog. Phys.* **2008**, *71*, 036601.
(35) Gonzalez, A. G.; Diez, J.; Gratton, R.; Gomba, J. *Europhys. Lett.* **2007**, *77*, 44001.
(36) Funston, A. M.; Novo, C.; Davis, T. J.; Mulvaney, P. *Nano Lett.* **2009**, *9*, 1651.